Supplemental Material for
A Superradiant Maser with Nitrogen-Vacancy Center Spins

Qilong Wu, Yuan Zhang,* and Xigui Yang
Henan Key Laboratory of Diamond Optoelectronic Materials and Devices,
Key Laboratory of Material Physics, Ministry of Education, School of Physics and Microelectronics,
Zhengzhou University, Daxue Road 75, Zhengzhou 450052 China

Shi-Lei Su
School of Physics and Microelectronics, Zhengzhou University, Daxue Road 75, Zhengzhou 450052 China

Chongxin Shan[†]
Henan Key Laboratory of Diamond Optoelectronic Materials and Devices,
Key Laboratory of Material Physics, Ministry of Education, School of Physics and Microelectronics,
Zhengzhou University, Daxue Road 75, Zhengzhou 450052 China

Klaus Mølmer[‡]
Aarhus Institute of Advanced Studies, Aarhus University,
Høegh-Guldbergs Gade 6B, DK-8000 Aarhus C, Denmark
Center for Complex Quantum Systems, Department of Physics and Astronomy,
Aarhus University, Ny Munkegade 120, DK-8000 Aarhus C, Denmark

CONTENTS

---

* yzhuaudipc@dipc.org
† cxshan@zzu.edu.cn
‡ moelmer@phys.au.dk

S1. ENERGY DIAGRAM OF NV⁻ CENTERS AND OPTICAL PUMPING

In this section, we provide more information on the energy diagram of NV⁻ centers in diamond. We present the pumping mechanism to create population inversion in the NV⁻ spin levels, and we demonstrate that the NV⁻ spins can be modeled as pseudo-1/2 spins for situation considered in the main text.

The energy diagram of the NV⁻ centers is shown in Fig.S1(a). The NV⁻ centers have one electronic ground state $^3A_2$ and three electronic excited states $^3E, ^1A_1, ^1E$. The spin triplet states $^3A_2, ^3E$ are split into one state $|0\rangle$ and one doublet $|\pm1\rangle$ with the spin projection number 0 and ±1 along the quantization axes, respectively. The other states $^1A_1, ^1E$ are spin singlet states. The NV⁻ centers can be laser-excited at 532 nm from the state $|0\rangle$ ($|\pm1\rangle$) of the $^3A_2$ state to the state $|0\rangle$ ($|\pm1\rangle$) of the ^3E, which is often accompanied by the creation and subsequent relaxation of lattice phonons. The excited NV⁻ centers can return back to the state $|0\rangle$ ($|\pm1\rangle$) of the $^3A_2$ state by light emission at the 637 nm zero-phonon line. In addition, the NV⁻ centers can decay non-radiatively from the $|\pm1\rangle$ components of the ^3E state through the intermediate state $^1A_1, ^1E$ to the $|0\rangle$ and $|\pm1\rangle$ states of the ground state $^3A_2$. The optical excitation and the radiative emission do not change the spin projection, while the non-radiative process introduces an effective decay from the spin projection ±1 to zero. Thus, by pumping the NV⁻ centers optically, we can create more population on the spin state $|0\rangle$ than on the other spin states $|\pm1\rangle$. In the presence of a strong magnetic field, the spin level $|-1\rangle$ can be shifted below the spin state $|0\rangle$, see Fig.S1(b), and in this case, the optical pumping creates a population inversion between the upper $|0\rangle$ and lower
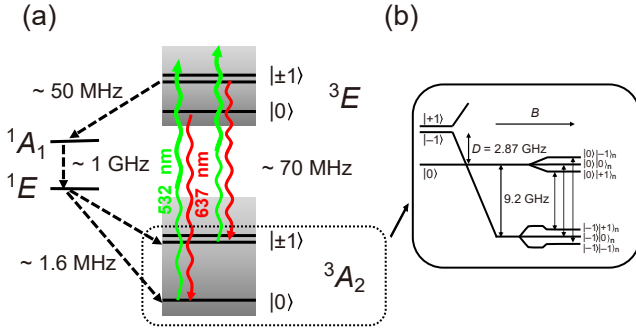
Figure S1. Energy diagram with optical and microwave transitions in NV$^-$ centers. Panel (a) shows the spin-triplet $^3A_2$, ^3E and spin-singlet $^1E, ^1A_1$ electronic states and the transitions driven by optical pumping by a laser with wavelength 532 nm, fluorescence at the 637 nm zero-phonon line, as well as non-radiative decay through the spin-singlet states (dashed lines). The rates of the various processes are listed next to the downward arrows, and the optical pumping and the decay process lead to an effective decay from the $|\pm1\rangle$ state to the $|0\rangle$ state. Panel(b) complements the panel (a) with the Zeeman-shifted electron spin levels ($|+1\rangle$ upwards, and $|-1\rangle$ downwards), and the Zeeman-shifted nitrogen-nuclear spin levels $|\pm1\rangle_n$ (the shifted direction depends on the electron spin levels) in the presence of a strong magnetic field, as well as the hyperfine interaction between the electron and nuclear spin. Note that the electron and nuclear spin levels $|0\rangle$, $|0\rangle_n$ are not affected by the magnetic field. Between the electron-nuclear spin states, there are three possible transitions, and we assume that only one of them is resonant to the resonator mode. See the text for more information.

$|-1\rangle$ spin level.

In the following, we give a detailed account of the energy shift of the electron spin states. We focus on the electronic ground state $^3A_2$, described by the Hamiltonian:

$$\hat{H}_e = g_e\mu_e\mathbf{B}\cdot\hat{\mathbf{S}} + D\left[\hat{S}_z^2 - \frac{1}{3}S\left(S+1\right)\right]. \quad (S1)$$

Here, $g_e \approx 2$ is the Lande g-factor and $\mu_e = 9.274\times10^{-24}$ J/T is the Bohr magneton. $\mathbf{B} = \sum_{i=x,y,z} B_i\mathbf{e}_i$ and $\hat{\mathbf{S}} = \sum_{i=x,y,z} \hat{S}_i\mathbf{e}_i$ are the applied static magnetic field and the electron spin vector in the Cartesian coordinate system (with the unit vectors $\mathbf{e}_i$), respectively. In the basis of the spin states $\{|+1\rangle, |0\rangle, |-1\rangle\}$, the x-, y- and z- component of the vector $\hat{\mathbf{S}}$ have the form

$$\hat{S}_x = \frac{1}{\sqrt{2}}\begin{pmatrix} 0 & 1 & 0 \\ 1 & 0 & 1 \\ 0 & 1 & 0 \end{pmatrix}, \hat{S}_y = \frac{1}{\sqrt{2}i}\begin{pmatrix} 0 & 1 & 0 \\ -1 & 0 & 1 \\ 0 & -1 & 0 \end{pmatrix},$$

$$\hat{S}_z = \begin{pmatrix} 1 & 0 & 0 \\ 0 & 0 & 0 \\ 0 & 0 & -1 \end{pmatrix}. \quad (S2)$$

Using the above expressions, we can rewrite the second

term of Eq.(S1) as

$$\frac{1}{3}D\begin{pmatrix} 1 & 0 & 0 \\ 0 & -2 & 0 \\ 0 & 0 & 1 \end{pmatrix}. \quad (S3)$$

This expression indicates that the state $|0\rangle$ has a frequency $-\frac{2}{3}D$ while the other states $|\pm1\rangle$ have the frequency $-\frac{1}{3}D$, leading to a transition frequency $D = 2\pi \times 2.87$ GHz in the absence of the magnetic field. The spin states $|\pm1\rangle$ are also split by local electric fields due to strain in the diamond matrix. Since this splitting is much smaller than the magnetic field-induced splitting as considered in the present article, we ignore it in the following discussion. However, we note that the former splitting might contribute also partially to the inhomogeneous broadening of the NV spin-ensemble.

In the room-temperature maser based on NV$^-$ spins [1], the triplet nuclear spin of nitrogen atoms plays also an important role. Thus, we need to complement the electron spin Hamiltonian given by Eq.(S1) with the nuclear spin Hamiltonian

$$\hat{H}_n = -g_n\mu_n\mathbf{B}\cdot\hat{\mathbf{I}} + \hat{\mathbf{S}}\overleftrightarrow{A}\hat{\mathbf{I}}. \quad (S4)$$

Here, g_n is the nuclear Lande g-factor, $\mu_n = \mu_e/1837$ is the nuclear Bohr magneton, $\hat{\mathbf{I}} = \sum_{i=x,y,z} \hat{I}_i\mathbf{e}_i$ is the nuclear spin operator. The nucleus is a spin-1 particle and it has three states $|+1\rangle_n, |0\rangle_n, |-1\rangle_n$. In the basis of these states, the components $\hat{I}_i$ have same structure as Eq.(S2). The second term of Eq.(S4) describes the hyperfine interaction with the uni-axially anisotropic tensor $\overleftrightarrow{A}$, which has the perpendicular $A_\perp = -2.7$ MHz and parallel component $A_\parallel = -2.1$ MHz with respect to the quantization axis.

To describe the quantum states of the electron and nuclear spin together, in principle, we should introduce nine product states $|s_e\rangle|s_n\rangle_n$ (with $s_e, s_n = 0, \pm1$) and diagonalize the total spin Hamiltonian $\hat{H}_s = \hat{H}_e + \hat{H}_n$. In view of large frequency difference between electron and nuclear momentum, it is, however, eligible to diagonalize first $\hat{H}_e$, and subsequently, for each electron spin eigenstate, diagonalize $\hat{H}_n$ among the nuclear spin states.

In the following, we consider the particular case, where $\mathbf{B}$ is parallel to the line between the vacancy and the nitrogen atom, see Fig.1(b) of the main text. In this case, Eq.(S1) can be easily diagonalized, and the energy of the spin state $|0\rangle$ is not changed, i.e. $\omega_0 = -\frac{2}{3}D$, while that of the spin states $|\pm1\rangle$ is given by $\omega_\pm = \frac{1}{3}D\pm g_e\mu_eB$ (with the magnetic field amplitude B). If the electron spin occupies the state $|0\rangle$, we can ignore the hyper-fine interaction and simplify Eq.(S4) as $\hat{H}_n = -g_n\mu_nB\hat{I}_z$. As a result, the product state $|0\rangle|0\rangle_n$ has the frequency $\omega_{00} = \omega_0$ and the states $|0\rangle|\pm1\rangle_n$ have the frequencies $\omega_{0\pm1} = \omega_0 \mp g_n\mu_nB$. If the electron spin occupies the state $|-1\rangle$, Eq.(S4) can be simplified as $-\left(g_n\mu_nB - A_\parallel\right)\hat{I}_z$. As a result, the product state $|-1\rangle|0\rangle_n$ has the frequency

$\omega_{-10} = \omega_-$ and the states $|-1\rangle |\pm 1\rangle_n$ have the frequencies $\omega_{-1\pm 1} = \omega_{-1} \pm (g_n \mu_n B - A_\parallel)$. This analysis leads to the energy scheme shown in Fig.S1 (b). Here, the presence of $A_\parallel$ makes the nuclear spin state $|+1\rangle_n$ have the highest energy. For the NV$^-$ centers subject to an arbitrary magnetic field, we expect a similar energy scheme as Fig.S1(b), however, with a more complex dependence of the energy levels on the magnetic field.

When the analysis is extended to multiple NV$^-$ centers, we have to account for that there are four possible orientations of the vacacny and the nitrogen atom. To maximize the Zeeman-shift for a given magnetic field, we can place the diamond in such way that the magnetic field is along one of these directions, see Fig.1(a,b) in the main text. In this case, the magnetic field along the other quantization axes, and thus the splitting of the corresponding spin levels, are small. If the microwave resonator has a narrow linewidth, it couples only to the spins with centers aligned along the magnetic field. Furthermore, for a strong magnetic field as considered in [1], the transitions between different electron-nuclear spin states, as indicated in Fig.S1(b), are well separated so that only one of them couples resonantly with the resonator mode. We assume that this simplification applies in this work so that we can treat the resonant transition as the pseudo-1/2 spins.

S2. SECOND-ORDER MEAN-FIELD EQUATIONS

In the main text, we outline the procedure to derive the equations for the physical observables in the second-order mean-field approach, and explain the equations for the mean photon number in the main resonator $\langle \hat{a}^\dagger \hat{a} \rangle$ and the spin-photon correlation $\langle \hat{\sigma}_k^\dagger \hat{a} \rangle$ and the mean photon number in the filter resonator $\langle \hat{b}^\dagger \hat{b} \rangle$, see Eq.(2), (3) and (4). In this section, we provide all the other equations needed for our calculations. The equation for the population difference $\langle \hat{\sigma}_k^z \rangle$ reads

$$\frac{\partial}{\partial t} \langle \hat{\sigma}_k^z \rangle = -i2g_k \left(\langle \hat{\sigma}_k^\dagger \hat{a} \rangle - \langle \hat{a}^\dagger \hat{\sigma}_k^- \rangle \right) \\ - \gamma_k \left[\left(2n_k^{th} + 1 \right) \langle \hat{\sigma}_k^z \rangle + 1 \right] - \eta_k \left(\langle \hat{\sigma}_k^z \rangle - 1 \right). \quad (S5)$$

The equation for the spin-spin correlation $\langle \hat{\sigma}_k^\dagger \hat{\sigma}_{k'}^- \rangle$ reads

$$\frac{\partial}{\partial t} \langle \hat{\sigma}_k^\dagger \hat{\sigma}_{k'}^- \rangle = i \left(\tilde{\omega}_k^* - \tilde{\omega}_{k'} \right) \langle \hat{\sigma}_k^\dagger \hat{\sigma}_{k'}^- \rangle \\ + i \left(g_{k'} \langle \hat{\sigma}_k^\dagger \hat{a} \rangle \langle \sigma_{k'}^z \rangle - g_k \langle \hat{\sigma}_k^z \rangle \langle a^\dagger \hat{\sigma}_{k'}^- \rangle \right). \quad (S6)$$

The equation for the photon-photon correlation $\langle \hat{a}^\dagger \hat{b} \rangle$

reads

$$\frac{\partial}{\partial t} \langle \hat{a}^\dagger \hat{b} \rangle = i \left(\tilde{\omega}_c^* - \tilde{\omega}_f \right) \langle \hat{a}^\dagger \hat{b} \rangle \\ + i \sum_k g_k \langle \hat{\sigma}_k^\dagger \hat{b} \rangle + iG \left(\langle \hat{b}^\dagger \hat{b} \rangle - \langle \hat{a}^\dagger \hat{a} \rangle \right), \quad (S7)$$

which depends on the correlations between the spins and the filter resonator $\langle \hat{\sigma}_k^\dagger \hat{b} \rangle$ (and the conjugation $\langle \hat{b}^\dagger \hat{\sigma}_k \rangle$). The equations for these correlations read

$$\frac{\partial}{\partial t} \langle \hat{\sigma}_k^\dagger \hat{b} \rangle = i \left(\tilde{\omega}_k^* - \tilde{\omega}_f \right) \langle \hat{\sigma}_k^\dagger \hat{b} \rangle - ig_k \langle \hat{a}^\dagger \hat{b} \rangle \langle \hat{\sigma}_k^z \rangle - iG \langle \hat{\sigma}_k^\dagger \hat{a} \rangle. \quad (S8)$$

S3. SUMMARY OF EXPERIMENTAL PARAMETERS

In Tab.S1, we summarize the parameters reported in several experiments on the microwave resonators (frequency ω_c, damping rate κ_c) and the NV$^-$ center spins (number of spins N, dephasing rate χ_k, single spin-resonator coupling g_k), as well as the combined parameters (the collective Rabi-frequency $\Omega = \sqrt{N}g_k$ and the Purcell-enhanced decay rate $\Gamma_c = 4g_k^2/\kappa_c$). If the parameter Ω is larger or smaller than κ_c and χ_k, the system works in the collective strong or weak coupling regime (see the the last line of Tab.S1). Note that the spin relaxation rate γ_k is usually orders of magnitude smaller than the dephasing rate χ_k and is thus usually not reported in the experiments. We can utilize the parameter Γ_c to estimate the orders of magnitude for the emission linewidth in the superradiant maser regime.

S4. SECOND-ORDER MEAN-FIELD EQUATIONS FOR SPIN SUB-ENSEMBLES

In Sec.IV A of the main text, we presented the emission spectra for the system of spin sub-ensembles representing the inhomogeneous broadening of the spins. To this end, we adopted the second-order mean-field equations given in Sec.III in the main text to the system with spin sub-ensembles labeled by α. To reduce the computational effort, we assume that the spins in each sub-ensemble are identical, and obtain the following equations for the quantities related to individual spin sub-ensembles and between spin sub-ensembles.

Ref.	1*	2	3	4	5	6
$\omega_c/2\pi$	9.22 GHz	3.18 GHz	2.69 GHz	2.90 GHz	2.87 GHz	3.12 GHz
$\kappa_c/2\pi$	0.3 MHz	13.8 MHz	0.8 MHz	0.8 MHz	1.5 MHz	3.82 MHz
N	4×10^{13}	1.5×10^{16}	2.5×10^{12}	10^{12}	10^{12}	10^{17}
$(\chi_k/2\pi)^{**}$	0.64 MHz	4.7 MHz	2.6 MHz	-	3 MHz	3 MHz
$g_k/2\pi$	0.11 Hz	0.051 Hz	12 Hz	12 Hz	12 Hz	0.07 Hz
$\Gamma_c/2\pi$	1.61×10^{-7} Hz	7.5×10^{-10} Hz	7.2×10^{-4} Hz	7.2×10^{-4} Hz	3.84×10^{-4} Hz	5.13×10^{-9} Hz
$\Omega/2\pi$	0.70 MHz	6.12 MHz	19 MHz	12 MHz	12 MHz	12 MHz
Regimes	Strong	Weak	Strong	Strong***	Strong	Strong

Table S1. Summary of experimental parameters for the microwave resonators (frequency ω_c, damping rate κ_c), the NV$^-$ center spins (number of spins N, dephasing rate χ_k, single spin-resonator coupling g_k), as well as the combined parameters (Purcell-enhanced decay rate Γ_c, collective spin-resonator coupling $\Omega = \sqrt{N}g_k$). The last line assigns the systems to either the regime of collective weak or strong coupling. $*$ marks the parameters (in the first column) used in our numerical simulations. $**$ indicates that the dephasing rate corresponds to half of the FWHM of the inhomogeneously broadened spin spectrum. $***$ marks that a dephasing rate was not reported in the experiment, and the strong coupling regime is deduced by using the typical value of the dephasing rate.

.

A. Equations Involving Main Resonator

The mean intra-resonator photon number follows the equation

$$\frac{\partial}{\partial t}\left\langle \hat{a}^\dagger \hat{a}\right\rangle = -\kappa_c \left\langle \hat{a}^\dagger \hat{a}\right\rangle + \kappa_c n_c^{th}$$
$$+ i\sum_\alpha N_\alpha g_\alpha \left(\left\langle \hat{\sigma}_{\alpha k}^\dagger \hat{a}\right\rangle - \left\langle \hat{a}^\dagger \hat{\sigma}_{\alpha k}^-\right\rangle\right), \qquad (S9)$$

where N_α, g_α denote the number of spins and the spin-resonator coupling of the α-th spin sub-ensemble, respectively. The spin-photon correlation $\left\langle \hat{\sigma}_{\alpha k}^\dagger \hat{a}\right\rangle$ follows the equation

$$\frac{\partial}{\partial t}\left\langle \hat{\sigma}_{\alpha k}^\dagger \hat{a}\right\rangle = i(\tilde{\omega}_{\alpha k}^* - \tilde{\omega}_c)\left\langle \hat{\sigma}_{\alpha k}^\dagger \hat{a}\right\rangle$$
$$- ig_{\alpha k}\left\langle \hat{a}^\dagger \hat{a}\right\rangle \left\langle \hat{\sigma}_{\alpha k}^z\right\rangle - i(g_{\alpha k}/2)\left(\left\langle \hat{\sigma}_{\alpha k}^z\right\rangle + 1\right)$$
$$+ ig_{\alpha k}\left\langle \hat{\sigma}_{\alpha k}^\dagger \hat{\sigma}_{\alpha k'}^-\right\rangle - i\sum_{\alpha'} N_{\alpha'} g_{\alpha'}\left\langle \hat{\sigma}_{\alpha k}^\dagger \hat{\sigma}_{\alpha' k'}^-\right\rangle. \quad (S10)$$

Here, we have defined $\tilde{\omega}_{\alpha k} = \omega_{\alpha k} - i\lambda_{\alpha k}^s$ with the total dephasing rate of pseudo-spins $\lambda_{\alpha k}^s = \frac{1}{2}\left[\gamma_{\alpha k}\left(2n_{\alpha k}^{th}+1\right)+\eta_{\alpha k}\right]+\chi_{\alpha k}$. In the last line of the above equation, the first and second term describe the spin-spin correlation in individual spin sub-ensembles and between the spin sub-ensembles, respectively. The population difference $\left\langle \hat{\sigma}_{\alpha k}^z\right\rangle$ and the spin-spin correlation

$\left\langle \hat{\sigma}_{\alpha k}^\dagger \hat{\sigma}_{\alpha' k'}^-\right\rangle$ follow the equations

$$\frac{\partial}{\partial t}\left\langle \hat{\sigma}_{\alpha k}^z\right\rangle = -i2g_\alpha \left(\left\langle \hat{\sigma}_{\alpha k}^\dagger \hat{a}\right\rangle - \left\langle \hat{a}^\dagger \hat{\sigma}_{\alpha k}^-\right\rangle\right)$$
$$- \gamma_{\alpha k}\left[\left(2n_{\alpha k}^{th}+1\right)\left\langle \hat{\sigma}_{\alpha k}^z\right\rangle + 1\right] - \eta_{\alpha k}\left(\left\langle \hat{\sigma}_{\alpha k}^z\right\rangle - 1\right), \quad (S11)$$
$$\frac{\partial}{\partial t}\left\langle \hat{\sigma}_{\alpha k}^\dagger \hat{\sigma}_{\alpha' k'}^-\right\rangle = i\tilde{\omega}_{\alpha k\alpha' k'}\left\langle \hat{\sigma}_{\alpha k}^\dagger \hat{\sigma}_{\alpha' k'}^-\right\rangle$$
$$+ i\left(g_{\alpha'}\left\langle \hat{\sigma}_{\alpha k}^\dagger \hat{a}\right\rangle \left\langle \hat{\sigma}_{\alpha' k'}^z\right\rangle - g_\alpha \left\langle \hat{\sigma}_{\alpha k}^z\right\rangle \left\langle \hat{a}^\dagger \hat{\sigma}_{\alpha' k'}^-\right\rangle\right). \quad (S12)$$

Here, the complex frequency is defined as $\tilde{\omega}_{\alpha k\alpha' k'} = \tilde{\omega}_{\alpha k}^* - \tilde{\omega}_{\alpha' k'}$.

To reduce the computational effort, we consider the steady-state version of the equations in the previous paragraph:

$$\left\langle \hat{a}^\dagger \hat{a}\right\rangle = i\sum_\alpha N_\alpha \frac{g_{\alpha k}}{\kappa_c}\left(\left\langle \hat{\sigma}_{\alpha k}^\dagger \hat{a}\right\rangle - \left\langle \hat{a}^\dagger \hat{\sigma}_{\alpha k}^-\right\rangle\right) + n_c^{th}, \quad (S13)$$

$$\left\langle \hat{\sigma}_{\alpha k}^z\right\rangle = \frac{-i2g_\alpha \left(\left\langle \hat{\sigma}_{\alpha k}^\dagger \hat{a}\right\rangle - \left\langle \hat{a}^\dagger \hat{\sigma}_{\alpha k}^-\right\rangle\right) + \eta_{\alpha k} - \gamma_{\alpha k}}{\gamma_{\alpha k}\left(2n_{\alpha k}^{th}+1\right)+\eta_{\alpha k}}, \quad (S14)$$

$$\left\langle \hat{\sigma}_{\alpha k}^\dagger \hat{\sigma}_{\alpha' k'}^-\right\rangle = \tilde{\omega}_{\alpha k\alpha' k'}^{-1}\left(g_{\alpha k}\left\langle \hat{\sigma}_{\alpha k}^z\right\rangle \left\langle \hat{a}^\dagger \hat{\sigma}_{\alpha' k'}^-\right\rangle\right.$$
$$\left. - g_{\alpha'}\left\langle \hat{\sigma}_{\alpha k}^\dagger \hat{a}\right\rangle \left\langle \hat{\sigma}_{\alpha' k'}^z\right\rangle\right), \quad (S15)$$

as well as

$$i(\tilde{\omega}_{\alpha k}^* - \tilde{\omega}_c)\left\langle \hat{\sigma}_{\alpha k}^\dagger \hat{a}\right\rangle = ig_\alpha \left(\left\langle \hat{a}^\dagger \hat{a}\right\rangle \left\langle \hat{\sigma}_{\alpha k}^z\right\rangle - \left\langle \hat{\sigma}_{\alpha k}^\dagger \hat{\sigma}_{\alpha k'}^-\right\rangle\right)$$
$$+ i\sum_{\alpha'} N_{\alpha'} g_{\alpha'}\left\langle \hat{\sigma}_{\alpha k}^\dagger \hat{\sigma}_{\alpha' k'}^-\right\rangle + i\frac{g_\alpha}{2}\left(\left\langle \hat{\sigma}_{\alpha k}^z\right\rangle + 1\right). \quad (S16)$$

Inserting Eq.(S13), (S14) and (S15) into Eq.(S16), we can obtain the self-consistent equations for the spin-photon correlations $\left\langle \hat{\sigma}_{\alpha k}^{\dagger} \hat{a} \right\rangle$ and $\left\langle \hat{a}^{\dagger} \hat{\sigma}_{\alpha k} \right\rangle$. Then, using the Find-Root program in the Mathematica, we can easily solve the coupled equations numerically for these correlations for systems with many spin sub-ensembles.

B. Equations Involving Filter Resonator

To compute the steady-state spectrum, the photon number $\left\langle \hat{b}^{\dagger} \hat{b} \right\rangle$ in the filter resonator still follows Eq.(4) in the main text, and the photon-photon correlation $\left\langle \hat{a}^{\dagger} \hat{b} \right\rangle$ and the spin-photon correlation $\left\langle \hat{\sigma}_{\alpha k}^{\dagger} \hat{b} \right\rangle$ follow the equations

$$\frac{\partial}{\partial t}\left\langle \hat{a}^{\dagger}\hat{b} \right\rangle = i\tilde{\omega}_{cf}\left\langle \hat{a}^{\dagger}\hat{b} \right\rangle + i\sum_{\alpha} N_{\alpha}g_{\alpha k}\left\langle \hat{\sigma}_{\alpha k}^{\dagger}\hat{b} \right\rangle$$
$$+ iG\left(\left\langle \hat{b}^{\dagger}\hat{b} \right\rangle - \left\langle \hat{a}^{\dagger}\hat{a} \right\rangle \right), \tag{S17}$$

$$\frac{\partial}{\partial t}\left\langle \hat{\sigma}_{\alpha k}^{\dagger}\hat{b} \right\rangle = i\tilde{\omega}_{\alpha kf}\left\langle \hat{\sigma}_{\alpha k}^{\dagger}\hat{b} \right\rangle - ig_{\alpha}\left\langle \hat{a}^{\dagger}\hat{b} \right\rangle\left\langle \hat{\sigma}_{\alpha k}^{z} \right\rangle - iG\left\langle \hat{\sigma}_{\alpha k}^{\dagger}\hat{a} \right\rangle. \tag{S18}$$

Here, we have introduced the complex frequency $\tilde{\omega}_{cf} = \omega_{c} - \omega_{f} + i\frac{1}{2}\left(\kappa_{c} + \kappa_{f} \right)$ and $\tilde{\omega}_{\alpha kf} = \omega_{\alpha k} - \omega_{f} + i\frac{1}{2}\left(2\lambda_{\alpha k}^{s} + \kappa_{f} \right)$.

To reduce the computational effort, we consider the steady-state solution of Eq.(S18) :

$$\left\langle \hat{\sigma}_{\alpha k}^{\dagger}\hat{b} \right\rangle = \tilde{\omega}_{\alpha kf}^{-1}\left(g_{\alpha}\left\langle \hat{a}^{\dagger}\hat{b} \right\rangle\left\langle \hat{\sigma}_{\alpha k}^{z} \right\rangle + G\left\langle \hat{\sigma}_{\alpha k}^{\dagger}\hat{a} \right\rangle \right). \tag{S19}$$

Inserting the above expression to Eq.(S17) , we get the steady-state photon-photon correlation

$$\left\langle \hat{a}^{\dagger}\hat{b} \right\rangle = G\frac{\left\langle \hat{a}^{\dagger}\hat{a} \right\rangle - \left\langle \hat{b}^{\dagger}\hat{b} \right\rangle - \sum_{\alpha}\tilde{\omega}_{\alpha kf}^{-1}N_{\alpha}g_{\alpha}\left\langle \hat{\sigma}_{\alpha k}^{\dagger}\hat{a} \right\rangle}{\tilde{\omega}_{cf} + \sum_{\alpha}\tilde{\omega}_{\alpha kf}^{-1}N_{\alpha}g_{\alpha}^{2}\left\langle \hat{\sigma}_{\alpha k}^{z} \right\rangle}. \tag{S20}$$

Inserting the above results to Eq.(4) in the main text, we get the steady-state mean photon number in the filter cavity

$$\left\langle \hat{b}^{\dagger}\hat{b} \right\rangle = \frac{G^{2}2\text{Im}\left[\frac{\left\langle \hat{a}^{\dagger}\hat{a} \right\rangle - \sum_{\alpha}\tilde{\omega}_{\alpha kf}^{-1}N_{\alpha}g_{\alpha}\left\langle \hat{\sigma}_{\alpha k}^{\dagger}\hat{a} \right\rangle}{\tilde{\omega}_{cf} + \sum_{\alpha}\tilde{\omega}_{\alpha kf}^{-1}N_{\alpha}g_{\alpha}^{2}\left\langle \hat{\sigma}_{\alpha k}^{z} \right\rangle} \right]}{G^{2}2\text{Im}\left[\tilde{\omega}_{cf} + \sum_{\alpha}\omega_{\alpha kf}^{-1}N_{\alpha}g_{\alpha}^{2}\left\langle \hat{\sigma}_{\alpha k}^{z} \right\rangle \right]^{-1} - \kappa_{f}}. \tag{S21}$$

C. Syncronization of Spin Subensembles

In Fig.2(b) of the main text, we observed a sharp emission peak with linewidth in the millihertz range for the system with fifty spin sub-ensembles when the incoherent pumping rate η_{k} exceeds the spin relaxation rate γ_{k}.
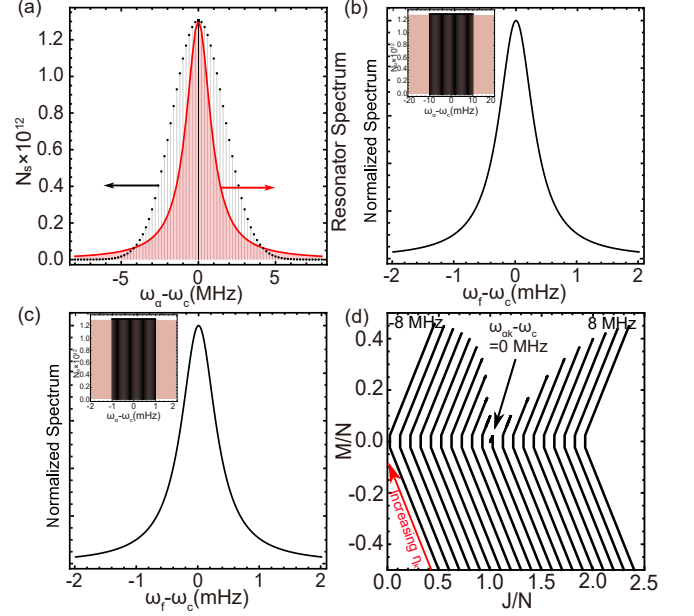

Figure S2. Supplemental results for spin subensembles. Panel (a) is similar to Fig.2(a) in the main text except that the single spin subensemble, which is at the center of Gaussian distribution and is ideally resonant to the resonator, splits into many subsubensembles. Panel (b) and (c) show that the spectrum with linewidth in the millihertz range does not change if the center subsubensembles spread about 20 mHz and 2 mHz wide (insets), respectively. Here, the total number of spins is 8×10^{13} and the spin pumping rate is $\eta_{k} = 10^{3}\gamma_{k}$. Panel (d) shows the evolution of the Dicke states of the individual spin subensembles with increasing pumping η_{k}, where the numbers mark the frequency detuning of the spin subensembles with respect to the resonator. For visualization purposes, we have considered 20 spin sub-ensembles here. The temperature is 25 mK, and other parameters are specified in the main text.

Fig.S2(a-c) show that this sharp emission peak persists even if we further discretize the center spin subensemble into many subsubensembles (see the insets). Here, we attribute the insensitivity of the spectrum to the synchronization effects of the sub-ensembles [7–9]. To support this, we look at the evolution of the Dicke states of spin sub-ensembles with increasing η_{k}, see Fig.S2(d). We see that the spin sub-ensembles nearly resonant to the resonator explore the Dicke states with low symmetry due to the balanced stimulated emission and absorption, while the spin sub-ensembles off-resonant to the resonator explore the Dicke states of higher symmetry close to the upper-right corner where the coupling with the resonator is reduced. These results suggest that all the spins within the inhomogeneous broadening are excited and contribute to the spectrum, while the spins closer to resonance with the resonator contribute more than the other sub-ensembles.

S5. SYSTEM WITH IDENTICAL SPINS

In the following, we present the simplified equations for the systems with identical spins. In this case, the mean photon number $\langle \hat{a}^\dagger \hat{a} \rangle$ follows the equation

$$\frac{\partial}{\partial t} \langle \hat{a}^\dagger \hat{a} \rangle = -\kappa_c \langle \hat{a}^\dagger \hat{a} \rangle + \kappa_c n_c^{th} + iNg_k \left(\langle \hat{\sigma}_k^\dagger \hat{a} \rangle - \langle \hat{a}^\dagger \hat{\sigma}_k^- \rangle \right),$$
(S22)

while the spin-photon correlation follows the equation

$$\frac{\partial}{\partial t} \langle \hat{\sigma}_k^\dagger \hat{a} \rangle = i \left(\tilde{\omega}_k^* - \tilde{\omega}_c \right) \langle \hat{\sigma}_k^\dagger \hat{a} \rangle - ig_k \langle \hat{a}^\dagger \hat{a} \rangle \langle \hat{\sigma}_k^z \rangle$$
$$- ig_k \frac{1}{2} \left(\langle \hat{\sigma}_k^z \rangle + 1 \right) - i \left(N - 1 \right) g_k \langle \hat{\sigma}_k^\dagger \hat{\sigma}_{k'}^- \rangle.$$
(S23)

Here, we have replaced the sum over spins $\sum_k$ with the factor N, and the sum of the spins coupled to any partiular spin $\sum_{k' \neq k}$ with the factor $N - 1$. The population difference $\langle \hat{\sigma}_k^z \rangle$ and the spin-spin correlation $\langle \hat{\sigma}_k^\dagger \hat{\sigma}_{k'}^- \rangle$ still follow Eq.(S5) and Eq.(S6), respectively.

The photon-photon correlation $\langle \hat{a}^\dagger \hat{b} \rangle$ follows the equation

$$\frac{\partial}{\partial t} \langle \hat{a}^\dagger \hat{b} \rangle = i \left(\tilde{\omega}_c^* - \tilde{\omega}_f \right) \langle \hat{a}^\dagger \hat{b} \rangle + iNg_k \langle \hat{\sigma}_k^\dagger \hat{b} \rangle$$
$$+ iG \left(\langle \hat{b}^\dagger \hat{b} \rangle - \langle \hat{a}^\dagger \hat{a} \rangle \right).$$
(S24)

The mean photon number $\langle \hat{b}^\dagger \hat{b} \rangle$ in the filter cavity and the spin-photon correlation $\langle \hat{\sigma}_k^\dagger \hat{b} \rangle$ still obey Eq.(4) in the main text and Eq.(S8), respectively.

S6. QUANTUM JUMPS AND COHERENT COUPLING AMONG DICKE STATES

To understand the system dynamics in the Dicke state representation, $|J, M\rangle$, we separately address the incoherent quantum jumps [10, 11] and the coherent coupling. The Dicke states are characterized by two integer or half-integer numbers $J = N/2, ..., 0$ and $M = -J, ...J$, and their energy levels are normally arranged in the way as shown in Fig.S3. Note that the levels for given J form a ladder with the spacing $\hbar\omega_k$, starting from $-J\hbar\omega_k$ and ending at $J\hbar\omega_k$. For convenience, the ladders for different J are shifted horizontally in the figure to form a triangular pattern (grey dashed lines for the boundary).

For the spin relaxation (blue arrows) with the rate $(1 + n_k^{th})\gamma_k$, the jumps occur towards the states with reduced M, and are dominated by the one towards the states with a smaller value of J (with large probability). Note that for the Dicke states with $M = -J$ (lowest rung of the Dicke ladders) jumps are only possible to the states with larger J due to the absence of states with $M < -J$. The upward quantum jumps for the spin pumping (red
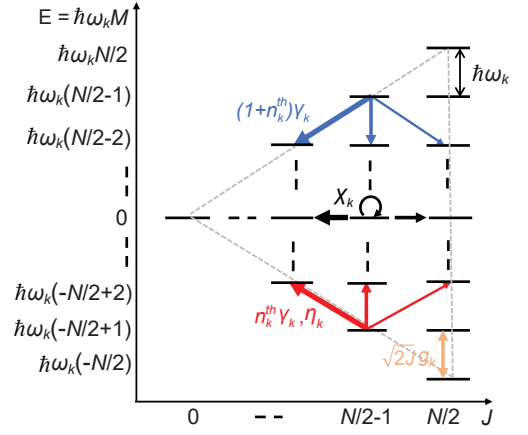

Figure S3. Relative probability (thickness of arrows) of the quantum jumps caused by the spin relaxation with rate $(1 + n_k^{th})\gamma_k$ (blue arrows), and the spin thermal or external pumping with rate $n_k^{th}\gamma_k, \eta_k$ (red arrows), as well as the spin dephasing with rate χ_k (black arrows), among the Dicke states (black horizontal lines, gray dotted lines for the boundary). The coherent and collective coupling with the resonator mode is shown by the orange arrow, and the coupling strength depends on J and M. Note that incoherent quantum jumps occur between two adjacent Dicke states with same or different J, while the coherent coupling occurs only between states with the same J. Here, the energy levels are for a spin-ensemble with an even number of spins. Energy levels for an odd number of spins are similar except that there are two levels for $M = \pm 1/2$.

arrows) with rate $n_s^{th}\gamma_k, \eta_k$ (thermal pumping or external pumping) are simply the vertical mirror of those for the spin relaxation process, while those for dephasing with rate χ_k occur among states with the same value of M. Coherent coupling with the resonator mode introduces reversible vertical transitions between adjacent Dicke states of same J (orange double-head arrow), with coupling strengths that increases with increasing J and decreasing $|M|$.

If only the spin relaxation occurs, the dynamics for the initially fully excited spin-ensemble $|J = N/2, M = J\rangle$ follows first the upmost rung of Dicke ladders $|J, M \approx J\rangle$ and then the lowest rung $|J, M \approx -J\rangle$, and ends up at the ground state $|J = N/2, M = -J\rangle$. If the spin-ensemble is initially in the ground state and subject only to incoherent excitation, this dynamics is merely reversed. If subject to only dephasing, the spin-ensemble in an initial Dicke state $|J, M\rangle$ follows the horizontal arrows towards the leftmost rung of Dicke ladders $(|J = |M|, M\rangle)$ with the same M. If subject only to the coherent coupling, the spin-ensemble initially in the ground state $|J = N/2, M = -J\rangle$, oscillates up and down along the ladder of states with $J = N/2$.

In the presence of all the processes, the dynamics becomes more complex and needs to be analyzed case by case. The simultaneous thermal-induced decay and excitation tend to cancel vertical motion, and their com-

bined effect is similar to the quantum jumps of the spin dephasing, ending up, however, at a non-inverted equilibrium excitation at the lower rung of the Dicke ladders with $J < N/2$ (see Fig.4 in the main text). When the external pumping η_k is included, the quantum jumps due to the spin pumping are enhanced and can overcome those due to the thermal decay, and the spin ensemble evolves towards the upper rung of the Dicke ladders with $J = M > 0$ (see Fig.4 in the main text). The tendency to occupy the upmost and lowest rung of the Dicke ladders is associated with the higher combinatorial degeneracy of these states and is further enforced by the dephasing process.

When adding the coherent coupling with the resonator mode, the system explores also the states in the middle of the Dicke ladders. For weak external pumping, the spin-ensemble is not population-inverted, and there are only few photons inside the resonator. As a result, the coherent coupling is relatively weak, and the dynamics is not affected so much. In contrast, for strong external pumping, the spin-ensemble becomes population-inverted, and the photon number inside the resonator increases dramatically due to the stimulated emission. The increase of the photon number increases also the stimulated absorption, which tends to balance the stimulated emission, leading to significant population of the middle of Dicke ladders. However, in the presence of large dephasing, the system finally occupies the upper rung of Dicke ladders with $J/N \approx M/N \approx 0$, see Fig.4 in the main text. Thus, except situations extremely near to the phase transition, the condition $|M| \approx J$ is satisfied in most cases, and the Holstein-Primakoff approximation discussed in Sec. S9 can be applied.

S7. DERIVATION OF TRANSITION BOUNDARIES

In the main text, we have observed the transitions between superradiance, superradiant maser and thermal regime. To understand the conditions leading to these transitions, in this section, we derive analytical expressions for these conditions. To this end, we focus on the stimulated processes and approximate Eq.(S23) as

$$\frac{\partial}{\partial t}\left\langle \hat{\sigma}_k^\dagger \hat{a} \right\rangle \approx i\left(\tilde{\omega}_k^* - \tilde{\omega}_c\right)\left\langle \hat{\sigma}_k^\dagger \hat{a} \right\rangle - ig_k\left\langle \hat{a}^\dagger \hat{a} \right\rangle \left\langle \hat{\sigma}_k^z \right\rangle. \quad \text{(S25)}$$

Next, we consider the steady-state solution of the above equation $\left\langle \hat{\sigma}_k^\dagger \hat{a} \right\rangle \approx \frac{g_k}{\tilde{\omega}_k^* - \tilde{\omega}_c}\left\langle \hat{a}^\dagger \hat{a} \right\rangle \left\langle \hat{\sigma}_k^z \right\rangle$, and obtain

$$\left\langle \hat{\sigma}_k^\dagger \hat{a} \right\rangle - \left\langle a^\dagger \hat{\sigma}_k^- \right\rangle \approx -i\frac{k_{EET}}{g_k}\left\langle \hat{a}^\dagger \hat{a} \right\rangle \left\langle \hat{\sigma}_k^z \right\rangle, \quad \text{(S26)}$$

where we have introduced the energy transfer rate $k_{EET} = \frac{2g_k^2(\lambda_k^s + \kappa_c/2)}{(\omega_k - \omega_c)^2 + (\lambda_k^s + \kappa_c/2)^2}$.

Inserting Eq.(S26) into the steady-state version of Eq.(S5), we obtain

$$\left\langle \hat{\sigma}_k^z \right\rangle \approx \frac{\eta_k - \gamma_k}{2k_{EET}\left\langle \hat{a}^\dagger \hat{a} \right\rangle + \gamma_k\left(2n_k^{th} + 1\right) + \eta_k}. \quad \text{(S27)}$$

Inserting Eq.(S26) in the steady-state version of Eq.(S27), we obtain

$$0 = -\kappa_c\left\langle \hat{a}^\dagger \hat{a} \right\rangle + \kappa_c n_c^{th} + Nk_{EET}\left\langle \hat{a}^\dagger \hat{a} \right\rangle \left\langle \hat{\sigma}_k^z \right\rangle. \quad \text{(S28)}$$

Using Eq.(S27), we can rewrite the above equation as $A\left\langle \hat{a}^\dagger \hat{a} \right\rangle^2 + B\left\langle \hat{a}^\dagger \hat{a} \right\rangle + C = 0$ with $A = 2k_{EET}$, $B = \gamma_k\left(2n_k^{th} + 1\right) + \eta_k - [2n_c^{th} + N(\eta_k - \gamma_k)/\kappa_c]k_{EET}$, $C = -n_c^{th}[(\gamma_k\left(2n_k^{th} + 1\right) + \eta_k]$. For our systems, $B^2 \gg AC$, we obtain the solution $\left\langle \hat{a}^\dagger \hat{a} \right\rangle = -B/A$. Assuming that the stimulated processes dominate over the thermal process $\left\langle \hat{a}^\dagger \hat{a} \right\rangle \geq n_c^{th}$, we obtain the condition for the incoherent pumping

$$\frac{\eta_k}{\gamma_k} \geq \frac{2n_k^{th} + 1 + N\mathcal{C}}{N\mathcal{C} - 1}, \quad \text{(S29)}$$

where we have introduced the single-particle cooperativity $\mathcal{C} = k_{EET}/\kappa_c$.

S8. SEMI-ANALYTICAL EXPRESSION FOR SPECTRAL PEAK POSITIONS AND LINEWIDTHS

In this section, we derive the semi-analytical expressions for the spectral peak positions and linewidths. To this end, we consider the steady-state solution of Eq.(S8)

$$\left\langle \sigma_k^\dagger \hat{b} \right\rangle = \tilde{\omega}_{kf}^{-1}\left(g_k\left\langle \hat{a}^\dagger \hat{b} \right\rangle \left\langle \hat{\sigma}_k^z \right\rangle + G\left\langle \hat{\sigma}_k^\dagger \hat{a} \right\rangle\right), \quad \text{(S30)}$$

with the complex frequency $\tilde{\omega}_{kf} = \omega_k - \omega_f + i\left(\lambda_k^s + \kappa_f/2\right)$. Inserting the above expression into Eq.(S24), we get the steady-state photon-photon correlation

$$\left\langle \hat{a}^\dagger \hat{b} \right\rangle = G\frac{\left\langle \hat{a}^\dagger \hat{a} \right\rangle - \left\langle \hat{b}^\dagger \hat{b} \right\rangle - \tilde{\omega}_{kf}^{-1} Ng_k\left\langle \sigma_k^\dagger \hat{a} \right\rangle}{\tilde{\omega}_{cf} + \tilde{\omega}_{kf}^{-1} Ng_k^2\left\langle \hat{\sigma}_k^z \right\rangle}, \quad \text{(S31)}$$

with the complex frequency $\tilde{\omega}_{cf} = \omega_c - \omega_f + i\frac{1}{2}\left(\kappa_c + \kappa_f\right)$. Inserting the above results into Eq.(4) of the main text, we get the steady-state mean photon number in the filter cavity

$$\left\langle \hat{b}^\dagger \hat{b} \right\rangle = \frac{G^2 2\text{Im}\left[\frac{\tilde{\omega}_{kf}\left\langle \hat{a}^\dagger \hat{a} \right\rangle - Ng_k\left\langle \hat{\sigma}_k^\dagger \hat{a} \right\rangle}{\tilde{\omega}_{kf}\tilde{\omega}_{cf} + Ng_k^2\left\langle \hat{\sigma}_k^z \right\rangle}\right]}{G^2 2\text{Im}\left[\tilde{\omega}_{cf} + \omega_{kf}^{-1} Ng_k^2\left\langle \hat{\sigma}_k^z \right\rangle\right]^{-1} - \kappa_f}. \quad \text{(S32)}$$

To resolve the spectrum with the filter resonator approach, we require κ_f to be smaller than the spectral feature to be resolved, and G to be small enough to reduce the backaction on the main resonator. By analyzing

the numerator and denominator of Eq.(S32), we find that the spectral peak positions and linewidths are mainly determined by the denominator. Assuming that the denominator can be written as the product $\tilde{\omega}_{kf}\tilde{\omega}_{cf} + Ng_k^2 \langle \hat{\sigma}_k^z \rangle \approx (\omega_f - \tilde{\omega}_+)(\omega_f - \tilde{\omega}_-)$, we obtain two complex frequencies $\tilde{\omega}_\pm = [\tilde{\omega}_k^* + \tilde{\omega}_c^* \pm \sqrt{(\tilde{\omega}_k^* - \tilde{\omega}_c^*)^2 - 4Ng_k^2 \langle \hat{\sigma}_k^z \rangle}]/2$.

For the weak pumping, we have $\langle \hat{\sigma}_k^z \rangle \approx 2M/N \approx -2J/N < 0$ and thus the solutions become $\tilde{\omega}_\pm = [\tilde{\omega}_k^* + \tilde{\omega}_c^* \pm \sqrt{(\tilde{\omega}_k - \tilde{\omega}_c)^2 + 8g_k^2 J}]/2$. These solutions result in two peaks in the spectra with frequencies and linewidths given by their real and imaginary parts. For strong pumping, we have the population inversion $\langle \hat{\sigma}_k^z \rangle > 0$, and in this case, one of the solutions has a smaller linewidth, and is responsible for masing.

In particular, for the resonant condition $\omega_c = \omega_k$, we obtain $\tilde{\omega}_\pm = \omega_c + i(\lambda_k^s + \kappa_c/2 \pm \sqrt{R})/2$ with the abbreviation $R = (\lambda_k^s - \kappa_c/2)^2 + 4Ng_k^2 \langle \hat{\sigma}_k^z \rangle$. For $R < 0$ or $\langle \hat{\sigma}_k^z \rangle < -(\lambda_k^s - \kappa_c/2)^2/(4Ng_k^2)$, we obtain $\tilde{\omega}_\pm = \omega_c \mp \sqrt{|R|}/2 + i(\lambda_k^s + \kappa_c/2)/2$. As a result, the spectrum shows two peaks centered around $\omega_c \mp \sqrt{|R|}/2$ (separated by $\sqrt{|R|}$) with the linewidth $\lambda_k^s + \kappa_c/2$. When $\langle \hat{\sigma}_k^z \rangle$ approaches zero for increasing pumping, $\sqrt{|R|}$ decreases and thus the two peaks approach each other and finally merge into one. When $R > 0$, $\tilde{\omega}_\pm$ have the same real part ω_c, but different imaginary part $(\lambda_k^s + \kappa_c/2 \pm \sqrt{R})/2$. As a result, the two peaks center around ω_c, and one peak has larger linewidth $(\lambda_k^s + \kappa_c/2 + \sqrt{R})/2$ and the other one has smaller linewidth $(\lambda_k^s + \kappa_c/2 - \sqrt{R})/2$ (corresponds to the masing).
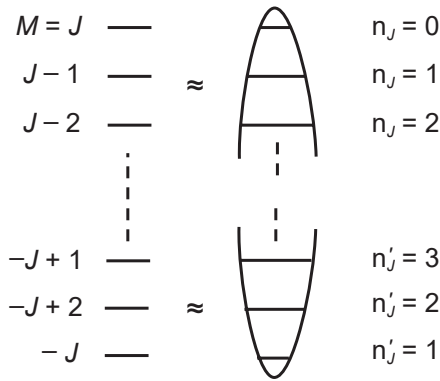

Figure S4. Approximation of Dicke states near the top and bottom of a Dicke ladder for given J (left) with the occupation number states of the upside-down and normal quantized harmonic oscillator (right).

S9. HOLSTEIN-PRIMAKOFF APPROXIMATION

In the main text, we have observed that the spin-ensemble occupies the upper and lower rung of Dicke ladders for strong and weak pumping, which is caused by the interplay of quantum jumps of the spin relaxation, spin pumping, spin dephasing and the coherent coupling with the resonator, as discussed in Sec. S6. Here we show that these situations allow us to derive approximate Hamiltonians for the spin ensemble-resonator coupling to understand the physics leading to the masing and the double peak spectrum, respectively. To this end, we consider the spin Hamiltonian $\hat{H}_s = (\hbar\omega_s/2)\sum_{k=1}^{N} \hat{\sigma}_k^z$ and the spin-resonator interaction $\hat{H}_{s-c} = \hbar g_s \left(\sum_k \hat{\sigma}_k^\dagger \hat{a} + a^\dagger \sum_k \hat{\sigma}_k^-\right)$ for the spins with identical frequency ω_s and identical coupling with the resonator g_s.

A. Parametric Coupling

To proceed, we apply the Holstein-Primakoff (HP) transformation to represent the Dicke states $|J, M\rangle$ with the occupation number states $|n_J\rangle$ of a quantized harmonic oscillator characterized by the creation $\hat{b}_J^\dagger$ and annihilation operator $\hat{b}_J$. The normal transformation assumes the relation $M = J - n_J$, which leads to the mapping $|J, M \pm 1\rangle \rightarrow |J, n_J \mp 1\rangle$ [12, 13] and thus to the relationships $\sum_k \sigma_k^z = 2\sum_J (J - \hat{b}_J^\dagger \hat{b}_J)$, $\sum_k \sigma_k^\dagger = \sum_J \sqrt{2J - \hat{b}_J^\dagger \hat{b}_J}\hat{b}_J$, $\sum_k \sigma_k^- = \sum_J \hat{b}_J^\dagger \sqrt{2J - \hat{b}_J^\dagger \hat{b}_J}$. In this case, the vacuum state $|n_J = 0\rangle$ is associated with the upper Dicke state $|J, J\rangle$ for given J. For the Dicke states with $n_J \ll 2J$, we have $\sqrt{2J - \hat{b}_J^\dagger \hat{b}_J}|n_J\rangle = \sqrt{2J - n_J}|n_J\rangle \approx \sqrt{2J}|n_J\rangle$ and thus $\sum_k \sigma_k^\dagger \approx \sum_J \sqrt{2J}\hat{b}_J$, $\sum_k \sigma_k^- \approx \sum_J \hat{b}_J^\dagger \sqrt{2J}$, which approximate effectively these Dicke states as the occupation number states of an inverted quantized harmonic oscillator (upper part of Fig.S4). Using these two relations, we can rewrite the spin-resonator interaction as the parametric coupling

$$\hat{H}_{s-c} \approx \hbar \sum_J \sqrt{2J}g_s \left(\hat{b}_J \hat{a} + \hat{a}^\dagger \hat{b}_J^\dagger\right). \qquad (S33)$$

In our system, the spin-ensemble occupies the upper rung of Dicke ladders for strong pumping, and thus the masing for strong pumping is well described by the parametric coupling of Eq.(S33). The parametric coupling leads to the gain and to spin-photon entanglement (two-mode squeezing) [14].

B. Spin-photon Dressed States

We can also apply the HP transformation $M = n_J' - J$ and the mapping $|J, M \pm 1\rangle \rightarrow |J, n_J' \pm 1\rangle$, which lead
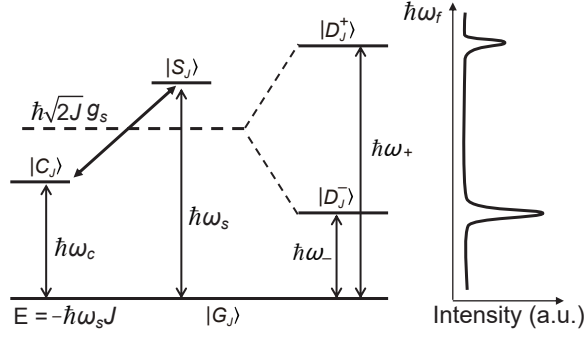
Figure S5. Formation of spin-photon dressed states. Left part shows the singly excited states $|C_J\rangle$ (with a single photon) and $|S_J\rangle$ (with a single spin excitation in the ensemble) with the mutual coupling $\hbar\sqrt{2J}g_s$ for given J. The middle part of the figure shows the dressed eigenstates $|D_J^+\rangle$, $|D_J^-\rangle$ (spin-photon dressed states), leading to the double peaks in the emission spectrum.

to the relations $\sum_k \hat{\sigma}_k^z = 2\sum_J(\hat{b}_J^\dagger \hat{b}_J - J)$, $\sum_k \hat{\sigma}_k^\dagger = \hat{b}_J^\dagger\sqrt{2J - \hat{b}_J^\dagger \hat{b}_J}, \sum_k \hat{\sigma}_k^- = \sqrt{2J - \hat{b}_J^\dagger \hat{b}_J}\hat{b}_J$. In this case, the vacuum state $|n'_J = 0\rangle$ is associated with the lowest Dicke state $|J, -J\rangle$ for any given J. For the Dicke states with $n'_J \ll 2J$, we have $\sum_k \hat{\sigma}_k^\dagger \approx \hat{b}_J^\dagger\sqrt{2J}, \sum_k \hat{\sigma}_k^- \approx \sqrt{2J}\hat{b}_J$. Using these two relations, we can rewrite the spin-resonator interaction as the coupling of two harmonic oscillators

$$\hat{H}_{s-c} \approx \hbar \sum_J \sqrt{2J}g_s\left(\hat{b}_J^\dagger \hat{a} + \hat{a}^\dagger \hat{b}_J\right). \qquad (S34)$$

In the low excitation limit, we can introduce the ground product state $|G_J\rangle = |n = 0\rangle |n'_J = 0\rangle$, and the singly excited states $|C_J\rangle = |n = 1\rangle |n'_J = 0\rangle$, $|S_J\rangle = |n = 0\rangle |n'_J = 1\rangle$, where $|n = 0\rangle$, $|n = 1\rangle$ are the vacuum state and single-photon state, and the labeling S, C distinguish the singly excited states with the excited spin-ensemble or the excited photon. Using these states, we can approximate $\hat{b}_J^\dagger \hat{a} \approx |S_J\rangle\langle C_J|$ and $\hat{a}^\dagger \hat{b}_J \approx |C_J\rangle\langle S_J|$, and thus obtain $\hat{H}_{s-c} \approx \hbar\sum_J \sqrt{2J}g_s\left(|S_J\rangle\langle C_J| + |C_J\rangle\langle S_J|\right)$. Furthermore, we can approximate the sum of the resonator Hamiltonian and the spin-ensemble Hamiltonian as $\hat{H}_c + \hat{H}_s \approx \hbar\sum_J[(\omega_c - \omega_s J)|C_J\rangle\langle C_J| - \omega_s(J-1)|S_J\rangle\langle S_J| - \omega_s J|G_J\rangle\langle G_J|]$. From these Hamiltonians we can obtain the energy levels and the coupling (for given J) as shown on the left side of Fig.S5.

After diagonalizing the approximate Hamiltonians for given J, we obtain the eigen-frequencies $d_\pm = \frac{1}{2}[\omega_c + \omega_s - 2J\omega_s \pm \sqrt{8Jg_s^2 + (\omega_c - \omega_s)^2}]$ for the dressed spin-photon states $|D_J^\pm\rangle = \frac{1}{N_\pm}[\omega_c - \omega_s \pm \sqrt{8Jg_s^2 + (\omega_c - \omega_s)^2}]|C_J\rangle + (2\sqrt{2J}g_s)|S_J\rangle$ with the normalization factors $N_\pm = \sqrt{16Jg_s^2 \pm (\omega_c - \omega_s)\sqrt{8Jg_s^2 + (\omega_c - \omega_s)^2}}$. The transition frequency between the dressed states and the ground state for given J can be readily calculated as $\omega_\pm = d_\pm - (-\omega_s J) = \frac{1}{2}[\omega_c + \omega_s \pm \sqrt{8Jg_s^2 + (\omega_c - \omega_s)^2}]$. The energy levels of the dressed states are shown in the middle of Fig.S5, and the transitions between them and the ground product state are responsible for the double-peak spectrum in the system with weak pumping, see the right side of Fig.S5. Furthermore, we note that $\omega_\pm$ are consistent with the real parts of $\tilde{\omega}_\pm$ as identified in Sec. S8. Note the relationship $J \approx -M = -\frac{1}{2}N\langle\hat{\sigma}_k^z\rangle$ for the weak pumping in our system.

[1] J. D. Breeze, E. Salvadori, J. Sathian, N. M. Alford, and C. W. M. Kay, Nature **555**, 493-496 (2018).

[2] A. Angerer, K. Streltsov, T. Astner, S. Putz, H. Sumiya, S. Onoda, J. Isoya, W. J. Munro, K. Nemoto, J. Schmiedmayer, and J. Majer, Nat. Phys. **14**, 1168-1172 (2018).

[3] S. Putz, D. O. Krimer, R. Amsüss, A. Valookaran, T. Nöbauer, J. Schmiedmayer, S. Rotter, and J. Majer, Nat. Phys. **10**, 720-724 (2014).

[4] R. Amsüss, C. Koller, T. Nöbauer, S. Putz, S. Rotter, K. Sandner, S. Schneider, M. Schramböck, G. Steinhauser, H. Ritsch, J. Schmiedmayer, and J. Majer, Phys. Rev. Lett. **107**, 060502 (2011).

[5] Y. Kubo, F. R. Ong, P. Bertet, D. Vion, V. Jacques, D. Zheng, A. Dréau, J. F. Roch, A. Auffeves, F. Jelezko, J. Wrachtrup, M. F. Barthe, P. Bergonzo, and D. Esteve, Phys. Rev. Lett. **105**, 140502 (2010).

[6] A. Angerer, T. Astner, D. Wirtitsch, H. Sumiya, S. On- oda, J. Isoya, S. Putz, and J. Majer, Appl. Phys. Lett. **109**, 033508 (2016).

[7] M. Xu, D. A. Tieri, E. C. Fine, J. K. Thompson, M. J. Holland, Phys. Rev. Lett. **113**, 154101 (2014).

[8] A. Shankar, J. Cooper, J. G. Bohnet, J. J. Bollinger, M. Holland, Phys. Rev. A **95**, 33423 (2017).

[9] K. Debnath, Y. Zhang, K. Mølmer, Phys. Rev. A **100**, 53821 (2019).

[10] Y. Zhang, Y.X. Zhang, and K. Mølmer, New J. Phys. **20**, 112001 (2018).

[11] Shammah, N., Ahmed, S., Lambert, N., De Liberato, S., and Nori, F., Phys. Rev. A **98**, 063815 (2018).

[12] J. A. Gyamfi, ArXiv:1907.07122 (2019).

[13] T. Holstein and H. Primakoff, Phys. Rev. **58**, 1098-1113 (1940).

[14] K. Debnath, Y. Zhang, and K. Mølmer, Phys. Rev. A **98**, 063837 (2018).